ADVANCED ENERGY MATERIALS
www.advenergymat.de

Rationally Designed Conversion-Type Lithium Metal Protective Layer for All-Solid-State Lithium Metal Batteries

*Haechannara Lim, Seunggoo Jun, Yong Bae Song, Ki Heon Baeck, Hongyeul Bae, Garam Lee, Jinhong Kim, and Yoon Seok Jung**

A stable interfacial design bridging Li metal and sulfide solid electrolytes is imperative for deploying practical all-solid-state Li metal batteries. Despite the extensive exploration of interlayer materials, including inorganic substances, lithiophilic metals, and their composites, a comprehensive understanding of their stability and chemo-mechanical evolution, particularly those influenced by cell fabrication processes, remains unexplored. Herein, it is meticulously investigate the formation and evolution of LiF, Mg, and conversion-type multicomponent MgF_2 ultrathin interlayers, each fabricated via thermal evaporation deposition. Unexpectedly, LiF and Mg fail to enhance cell performance, with LiF notably susceptible to external pressures during cell fabrication, leading to serious current constriction, while Mg deposition results in the formation of a Li-rich solid solution. Remarkably, the MgF_2 coatings demonstrate substantially superior performance in both Li|Li_6PS_5Cl|Li symmetric cells (up to 2000 h) and $LiNi_{0.70}Co_{0.15}Mn_{0.15}O_2$|$Li_6PS_5Cl$|Li full-cells (82% capacity retention after 800 cycles) at 30 °C. These results are attributed to the in-situ formation of LiF and Li_xMg nanograins through a conversion reaction, which, after repeated cycling, maintains stability and a fixed position at the interface while ensuring uniform interfacial Li^+ flux. Supported by comprehensive analyses, these findings highlight the pivotal role of conversion-type interlayers in mitigating side reactions and preventing Li penetration.

1. Introduction

All-solid-state Li metal batteries (ASLMBs) employing inorganic solid electrolytes (SEs) have emerged as a promising alternative, owing to their potential to outperform the peak energy density (≈300 Wh kg^{-1}) attainable with conventional lithium-ion batteries.[1–3] This advancement is realized by incorporating lithium metal anodes (LMAs), which possess the highest theoretical capacity (3860 mA h g^{-1}) and the lowest potential (−3.04 V vs normal hydrogen electrode).[4–7] Among the various SE classes,[8–16] sulfide SEs (SSEs), particularly Li argyrodite (e.g., Li_6PS_5Cl (LPSCl)), stand out because they provide excellent room-temperature ionic conductivities reaching up to 10^{-2} S cm^{-1} and exhibit mechanical deformability, making them favorable in practical applications.[7,12,17]

However, ASLMBs incorporating SSEs are hindered by two major challenges: aggressive reactivity between LMAs and SSEs and Li dendritic growth.[2,18–22] Owing to their narrow electrochemical stability window, SSEs undergo reductive decomposition and form passivating solid electrolyte interphases (SEIs) upon direct contact with Li metal.[2,23] The continuous growth of these poor ion-conducting layers ultimately escalates cell impedance, consequently impairing the cycle life of ASLMBs. SEI formation reduces the effective contact area, inducing current constriction and potentially accelerating dendritic Li growth.[2,18,19,23–26] Furthermore, factors such as inhomogeneous Li–SSE interfaces, non-uniform Li plating/stripping behaviors, and physical defects in the SSE properties (e.g., void spaces or cracks, insufficiently low electronic conductivity, and non-uniform local electronic structures) promote dendritic Li growth, which can precipitate sudden cell failure due to internal short circuits (ISCs).[20,21,27–32]

Surface modification strategies aimed at LMAs have been widely adopted to enhance interfacial stability, with Li-containing inorganic compounds and lithiophilic metals emerging as top contenders for interlayer applications.[33–38] First, inorganic materials (e.g., LiF, LiI, Li_3N) can potentially mitigate Li dendritic growth owing to their high interfacial energy with the Li metal and robust mechanical properties.[33–35,39] In particular, LiF has been extensively investigated as an inorganic interlayer due to its extremely low electronic conductivity (≈10^{-10} S cm^{-1}), known to foster favorable passivation in ASLMB cells.[40] Nonetheless, its notably low ionic conductivity of 10^{-9}–10^{-11} S cm^{-1} may restrict its use to ultrathin layers at the nanometer level.[41,42] Notably, the pronounced thinness, coupled with the embedded nature of

H. Lim, S. Jun, Y. B. Song, K. H. Baeck, Y. S. Jung
Department of Chemical and Biomolecular Engineering
Yonsei University
Seoul 03722, Republic of Korea
E-mail: yoonsjung@yonsei.ac.kr
H. Bae, G. Lee, J. Kim
POSCO N.EX.T Hub LiB Materials R&D Lab. LiB Materials Research Center
POSCO HOLDINGS
Pohang-si 37673, Republic of Korea

The ORCID identification number(s) for the author(s) of this article can be found under https://doi.org/10.1002/aenm.202303762

DOI: 10.1002/aenm.202303762

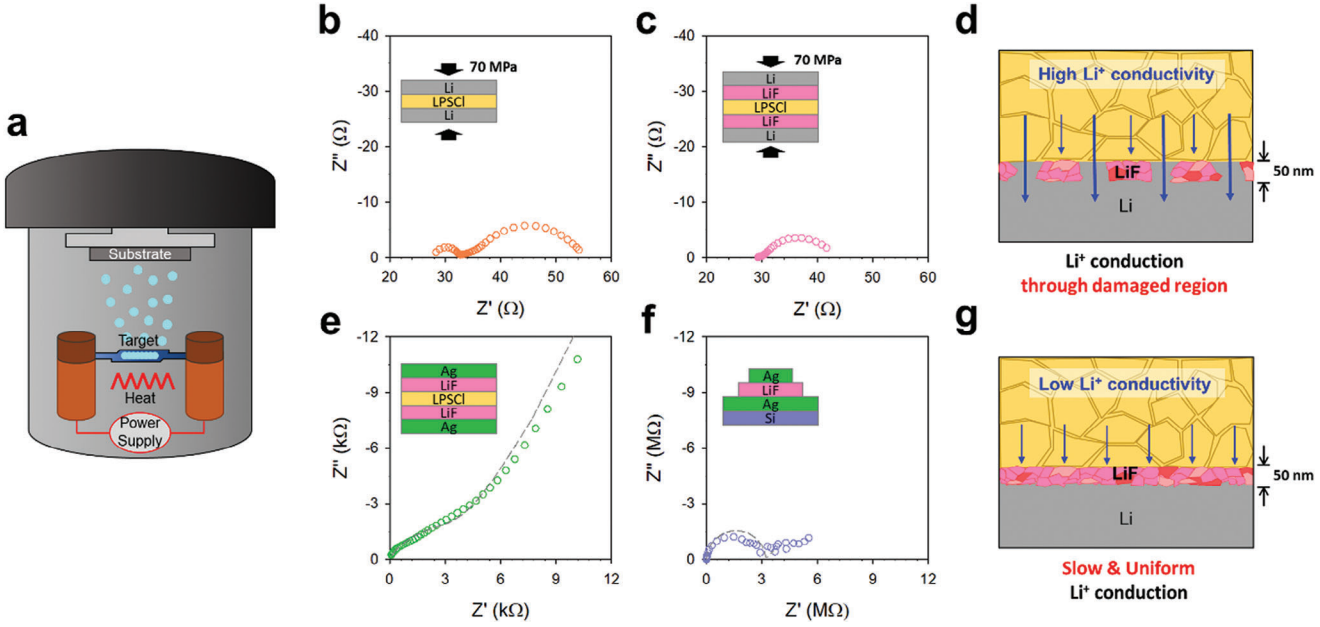

Figure 1. Ionic conductivity measurements of LiF at 30 °C. a) Schematic of thermal evaporation deposition process. Nyquist plots of Li|LPSCl|Li Li^+-non-blocking symmetric cells with b) bare and c) LiF-coated Li metal electrodes—fabricated at 70 MPa. d) Schematic of interfacial Li^+ transport through damaged LiF layer. e) Nyquist plot of Ag|LPSCl|Ag Li^+-blocking symmetric cell with 250 nm-thick LiF-coated LPSCl layer—fabricated under minimal pressures. f) Nyquist plot of Ag|LiF|Ag Li^+-blocking symmetric cell fabricated under no external pressures. Dashed lines in e) and f) are fitted lines using equivalent circuits. g) Schematic of uniform interfacial Li^+ transport through ideal, undamaged, and conformal LiF layer.

the LiF interlayer in ASLMBs, may overlook various aspects of its application (e.g., endurance to external pressure and coating conformability). Results presented herein from ASLMBs, employing an ultrathin LiF interlayer, exhibited no marked enhancement in performance, contradicting the general expectation regarding the positive impact of LiF layers.[33,39] Furthermore, despite its low Li^+ ion conductivity, no evident LiF-induced polarization was observed. A detailed discussion is provided in the Results and Discussion section. Despite the abundance of literature on LiF interlayers,[43,44] a precise characterization has largely been absent.

Metallic coatings, such as Al, Au, Ge, and In, have also been proposed as interlayers. Metallic interlayers can homogenize the Li^+ flux and suppress void formation at the LMA-SSE interfaces, attributed to several factors, such as increased Li diffusivity in the alloy phases and/or the geometrically stable property of the alloy phases.[36–38,45] Beyond regulating the Li^+ flux, metallic interlayers shield the Li metal from direct contact with SSEs, significantly attenuating side reactions.[38] Nevertheless, the chemical diffusion of metal elements within the metallic interlayers and repeated volume changes upon cycling weaken the interfacial coverage, posing challenges to long-term cyclability.[38,46,47] In a context highly relevant to the enhancement mechanisms facilitated by metallic interlayers, Mg-Li alloys have garnered considerable attention. With a high solubility of up to ≈70 at.% in Li, the Mg-Li alloy maintains phase stability over a wide alloy composition range, while its relatively high Li diffusion coefficient ensures fast Li^+ flux.[48–50] Furthermore, studies have demonstrated that the mechanical properties of Mg-Li alloys help maintain stable and/or uniform interfacial contact with SEs.[51,52]

Furthermore, bifunctional or multicomponent layers comprising robust inorganic materials and lithiophilic metals have been explored to overcome the inherent drawbacks of individual materials.[43,44,53] Combinations of LiF and alloying metals are prominent examples. Lee et al. introduced an Ag-LiF double-layer coating,[43] whereas Wang et al. fabricated functional-gradient LMAs through the reaction of AlF_3 with molten Li.[44] Concurrently, Wan et al. employed dual-salt electroless formation to establish LiF-Li_xMg bifunctional interphase.[53] Although these double-layer coatings or chemical-reaction-based multicomponent Li modification strategies have demonstrated prolonged cycle life and high current endurance when coupled with oxide SEs,[43,44] applications and exploration of SSEs have been scarcely reported. It is imperative to note the pronounced gap between the frequent application of common protective layers and their fundamental understanding. A comprehensive understanding of their formation, configuration, and evolution, as well as their impact on the electrochemical performance of ASLMBs, remains limited.

In this work, we present a comparative study on the formation and evolution of three representative protective interlayer categories on Li metal–inorganic (LiF), metallic (Mg), and conversion reaction-based multicomponent design (MgF_2), each prepared via thermal evaporation deposition (**Figure 1a**). Photographs of LiF-, Mg-, and MgF_2-deposited LMAs are presented in Figure S1 (Supporting Information). Contrary to conventional expectations, modifications utilizing LiF or Mg did not enhance the performance of the ASLMB. The first key finding revealed the substantial vulnerability of the LiF interlayer to external pressures, which induced pronounced current constriction through the damaged interface regions; instead of forming a distinct layer, Mg

deposition resulted in a gradient solid solution. In contrast, uniform MgF_2 coatings onto LMAs were obtained, leading to significantly enhanced performances in both Li|Li_6PS_5Cl|Li symmetric cells and $LiNi_{0.70}Co_{0.15}Mn_{0.15}O_2$ (NCM)|Li_6PS_5Cl|Li full-cells at 30 °C, attributed to the in situ formed interlayers, comprising LiF and Li_xMg nanograins through a conversion reaction.[54,55] These interlayers can regulate the uniform Li^+ flux, in contrast to the LiF layer. Additionally, detailed interfacial evolution was characterized by complementary analyses using electrochemical impedance spectroscopy (EIS), ex-situ X-ray photoelectron spectroscopy (XPS), ex-situ scanning electron microscopy (SEM), and operando electrochemical pressiometry analysis (OEP) measurements.

2. Results and Discussion

The pressurization-based cell fabrication process induces the mechanical deformation of soft and flexible LMAs. Specifically, Li metal tends to deform to conform to rough SE pellet surface and/or fill its pores (Figure S2, Supporting Information). Such deformation might lead to the formation of cracks in cell components. In particularly, inorganic interlayers are susceptible to damage owing to their inherent lack of flexibility, often overlooked. Guided by this understanding, control experiments were devised to validate the effects of external pressure on the conformality of the LiF interlayer.

First, EIS measurements were conducted for Li|LPSCl|Li symmetric cells with both bare and 50-nm-thick LiF-coated electrodes—fabricated under an external pressure of 70 MPa. Figure 1b,c shows the Nyquist plots at 30 °C for both bare and LiF-coated LMAs. The intercept values on the x-axis at high frequencies, corresponding to the resistance of the LPSCl layer, were comparable to one another and consistent with the Li^+ conductivity of LPSCl (2.5 mS cm^{-1} with a thickness of 750 µm corresponds to a resistance of 30 Ω). Given the reported extremely low Li^+ conductivity of 10^{-9}–10^{-11} S cm^{-1}, each 50 nm LiF layer in the cell should result in an increase of 3.8–380 kΩ.[41,42] Nonetheless, the interfacial resistance—corresponding to the overall amplitudes of the semicircle—was lower for LiF-coated LMAs than for bare LMAs, as detailed in the fitted values with the equivalent circuit in Figure S3, (Supporting Information) summarized in Table S1 (Supporting Information). This result contradicts previous reports that showed an evident increase in the resistance of LiF-coated SE pellets compared with that of bare SE pellets, where no external pressures were applied during cell preparation (a detailed discussion is provided in Supporting Information).[43,44] The even smaller interfacial resistance with the LiF interlayer in our results strongly suggests possible damage to the LiF interlayer during pressurization at 70 MPa, which could induce partial direct contact between LPSCl and Li metal, as illustrated in Figure 1d.

To validate this hypothesis, two additional control experiments using Li^+-blocking symmetric cells were performed to ensure that the LiF layer could be sustained with minimal or no external pressure. An Ag|LPSCl|Ag cell was prepared by depositing 250 nm LiF on a pre-pressurized LPSCl pellet, followed by Ag deposition via sputtering. The assembly was then placed in contact with two Ti rods as current collectors under minimal pressure. The corresponding Nyquist plot is shown in Figure 1e, while the corresponding Li^+ conductivity of LiF was estimated as 5.0×10^{-9} S cm^{-1} (details can be found in Figure S4, Supporting Information). Another cell with no external pressure, Ag|LiF|Ag, using a Si wafer as a flat substrate, was prepared by depositing 2 µm LiF on an Ag-coated Si wafer, followed by Ag coating. Electrical contacts were then fabricated by coating with Ag paste, through which the conductivity of the LiF layer was obtained without external pressure or physical stress. The resulting Nyquist plot, displayed in Figure 1f, corresponds to a conductivity value of approximately 1.7×10^{-11} S cm^{-1}, consistent with reported data (the corresponding equivalent circuit is shown in Figure S3, Supporting Information),[41,42] reflecting the mechanically intact LiF layer in the pressure-free cell (Figure 1g). These control experiments unequivocally revealed that the LiF interlayers in the Li|LPSCl|Li cells were severely damaged during the pressurization-based cell fabrication process, thereby highlighting the limitations in fully realizing their potentially beneficial effects in practical applications, as illustrated in **Figure 2**a(i). The top surface SEM images with corresponding EDXS elemental maps for LiF-coated LMAs before and after pressurization (Figure S5a,b, Supporting Information) visually confirm the mechanical damage to the LiF layer due to external pressures.

An attempt to construct an Mg interlayer via thermal evaporation deposition was not effective. During the evaporation process, the thermally evaporated Mg metal diffused into the bulk Li metal, forming Li-rich solid solutions instead of a distinct layer, as illustrated in Figure 2b(ii), explained by the highly favorable alloying reaction or fast diffusion of Mg into the Li metal.[49,56] More details are discussed later.

From these results, an MgF_2 interlayer subjected to in situ conversion and alloying reactions to form LiF and Li_xMg nanograins (Equations 1 and 2, respectively) may be beneficial. First, uniformly distributed LiF nanodomains can suppress the agglomeration or diffusion of Mg,[54] thereby immobilizing the Mg nanograins within the interface.

$$2Li + MgF_2 \rightarrow Mg + 2LiF \quad (1)$$

$$xLi + Mg \rightarrow Li_xMg \quad (2)$$

Second, the evenly distributed Li_xMg grains at the nanoscale enable a uniform Li^+ flux through the interfacial area, unlike with the LiF interlayer, where substantial current constriction occurs through mechanically damaged regions. Finally, even if the MgF_2 interlayer is damaged by uniaxial pressing, Li metal permeating through MgF_2 may participate in inducing the conversion reaction, thereby potentially facilitating partial healing of defects within the interlayer, as depicted in Figure 2a(iii).

Figure 2b presents the top-surface SEM image and corresponding energy dispersive X-ray spectroscopy (EDXS) elemental maps of the MgF_2-deposited LMAs. Comparative data for the LiF- and Mg-deposited LMAs are shown in Figures S5a,c (Supporting Information). The target thicknesses of the LiF, Mg, and MgF_2 coatings on the 30-µm-thick Li metal were set at 50, 35, and 50 nm, respectively, based on the thickness monitor of the thermal evaporation system, consistent with the ellipsometry analysis results (Figure S6, Supporting Information). The LiF and MgF_2 coating layers displayed significant conformability on the Li metal, whereas the Mg-deposited surface failed to present a

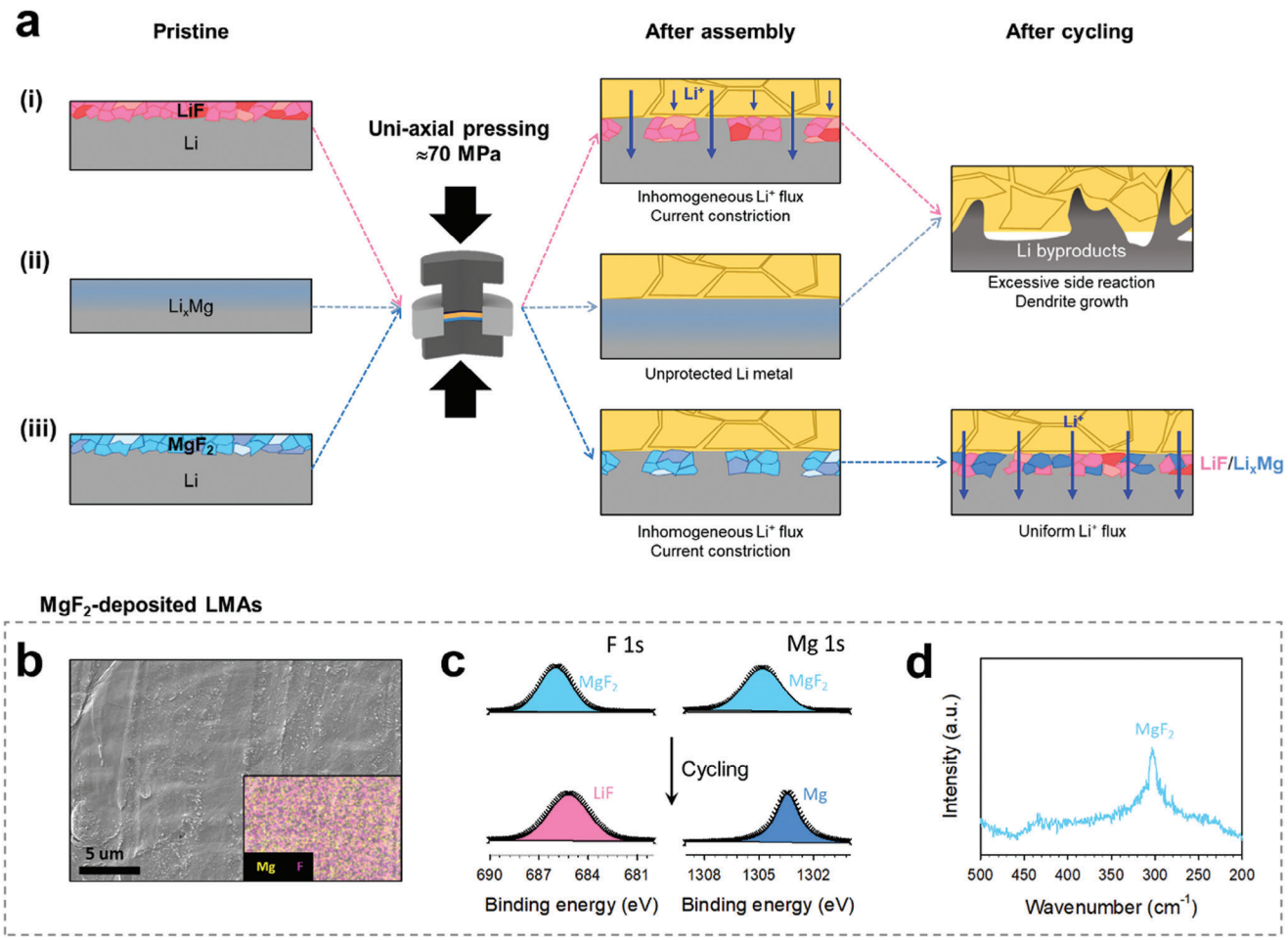

Figure 2. Characterization of LMAs with thermal evaporation deposited interlayers. a) Schematic of formation and evolution of (i) LiF, (ii) Mg, and (iii) MgF_2 in the pristine state, after cell assembly, and after cycling. b) Top surface SEM image with corresponding EDXS elemental maps of Mg and F for MgF_2-coated LMAs. c) Ex situ XPS signals of F 1s and Mg 1s of MgF_2-coated LMAs before (top) and after (bottom) galvanostatic cycling. d) Raman spectrum of MgF_2-coated LMAs.

distinct Mg signal on the EDXS map, indicating Mg diffusion into bulk Li. Subsequent characterizations of the three sample electrodes were performed using XPS. Figure 2c displays the F 1s and Mg 1s spectra of MgF_2-coated LMAs before and after cycling Li|LPSCl|Li symmetric cells at 30 °C. In the pristine state, peaks of F 1s and Mg 1s spectra at 685.75 and 1304.95 eV, respectively, matched well with those for MgF_2.[57] Additionally, the Raman spectrum exhibiting a peak centered at 303 cm^{-1} confirmed the successful deposition of MgF_2 (Figure 2d).[58] After 10 cycles at 0.2 mA cm^{-2} with 0.2 mA h cm^{-2}, both the F 1s and Mg 1s XPS spectra exhibited negative shifts to 685.1[44] and 1303.4 eV,[59] respectively, where LiF and metallic Mg (Li-Mg alloy) were adequately fitted. The LiF-deposited electrode exhibited a clear LiF peak at 686 eV in the F 1s spectrum (Figure S7a, Supporting Information), whereas the Mg-deposited LMAs exhibited only a broad and weak peak of metallic Mg at 1303.4 eV in the Mg 1s spectrum (Figure S7b, Supporting Information), indicating substantial diffusion of Mg metal into bulk Li. To confirm the presence and diffusion of Mg during alloying, time-of-flight secondary ion mass spectrometry (TOFSIMS) and dynamic secondary ion mass spectrometry (DSIMS) depth profiling were conducted. Figure S8a (Supporting Information) clearly indicates the presence of Mg (≈24 atomic mass units (amu)) in the mass spectrum. Additionally, Figure S8b (Supporting Information) reveals the diffusion of Mg into a range spanning tens of nanometers, evidenced by the decreasing slope of ^{24}Mg intensity in the DSIMS depth profile. An additional control experiment involving Mg deposition on a Cu substrate also corroborates the rapid diffusion of Mg into Li metal, as shown in Figure S9 (Supporting Information).

The electrochemical performance of LiF-, Mg-, and MgF_2-deposited LMAs was assessed by cycling Li|LPSCl|Li symmetric cells at 30 °C, with results summarized in **Figure 3**. The optimal thickness of MgF_2 coating was determined through critical current density (CCD) test results,[60] incrementing both the current density and cycling capacity by 0.1 mA cm^{-2} and 0.1 mA h cm^{-2}, respectively (Figure 3a; Figure S10, Supporting Information), setting on 50 nm. All electrodes underwent 10 cycles at 0.1 mA cm^{-2} with 0.1 mA h cm^{-2} in advance to ensure the successful conversion reaction of MgF_2. Specifically, the CCD results for MgF_2 coating thicknesses of 20, 30, 50, 70, and 100 nm are detailed in Figure 3a and Figure S10 (Supporting Information).

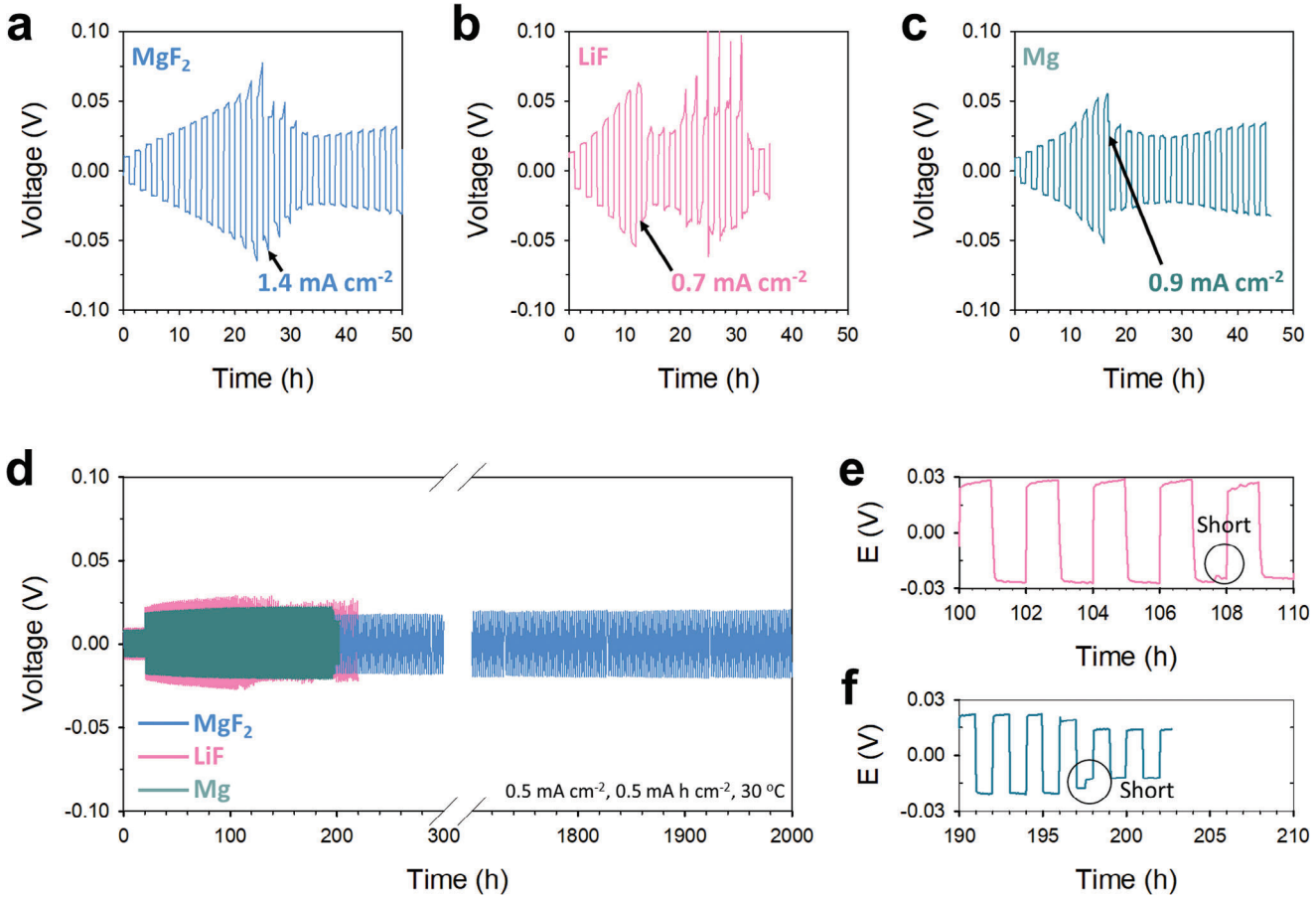

Figure 3. Electrochemical characterization using Li|LPSCl|Li cells at 30 °C. CCD (critical current density) test results for a) MgF_2-, b) LiF-, and c) Mg-deposited LMAs. Both current density and cycling capacity were incrementally increased, starting from 0.1 mA cm^{-2} and 0.1 mA h cm^{-2}, respectively, with increments of 0.1 mA cm^{-2} and 0.1 mA h cm^{-2}. d) Galvanostatic cycling test results at 0.2 mA cm^{-2} with 0.2 mA h cm^{-2} for the initial 10 cycles, and 0.5 mA cm^{-2} with 0.5 mA h cm^{-2} for the subsequent cycles. Corresponding enlarged views displaying the points of soft short circuit occurrences of e) LiF- and f) Mg-deposited LMAs.

The thinnest 20 nm coating exhibited a CCD value of only 0.3 mA cm^{-2}, even lower than that of bare Li metal (Figure S11, Supporting information). This lower performance is due to the noticeable non-uniformity of the coating, confirmed by TOFSIMS results (Figure S12a, Supporting Information). Conversely, the 50 nm coating demonstrated markedly improved conformality (Figure S12b, Supporting Information) and achieved the highest CCD value of 1.4 mA cm^{-2}. However, coatings that are too thick (70 and 100 nm) recorded lower CCD values, which is explained by the increased resistance caused by the excessive formation of insulating LiF.

Given an optimal MgF_2 thickness of 50 nm, the target coating layer thicknesses of LiF and Mg were set to 50 and 35 nm, respectively, to allow for a fair comparison (comprehensive calculations are available in the Supporting Information). The CCD test results for the MgF_2-coated LMAs (Figure 3a) were compared with those for the LiF- and Mg-deposited LMAs (Figure 3b,c, respectively). MgF_2-coated LMAs achieved the highest CCD value of 1.4 mA cm^{-2}, whereas LiF- and Mg-deposited samples encountered a sudden voltage drop beneath 0.8 and 1.0 mA cm^{-2}, respectively. Galvanostatic cycling tests were conducted at 0.5 mA cm^{-2} with 0.5 mA h cm^{-2} for each charge and discharge, with results displayed in Figure 3d–f. LiF- and Mg-deposited LMAs exhibited ISCs after ≈150 and ≈200 h, respectively, performing comparably or even worse than the bare LMAs (Figure S11, Supporting Information). A close examination of the voltage profiles revealed that the LiF-deposited LMAs exhibited an unstable voltage profile after ≈107 h (Figure 3e), likely correlating to the mechanical damage of the LiF interlayer during pressurization. Moreover, the Mg-deposited LMAs displayed an abrupt voltage drop at ≈197 h (Figure 3f), indicating minimal protection of the Li metal owing to the diffusion of Mg into the bulk Li. In contrast, the MgF_2-coated LMAs demonstrated the lowest overpotential and extended cycle life of up to 2000 h (Figure 3d).

To further understand the superior performance of MgF_2-coated LMAs over their LiF- or Mg-deposited counterparts, EIS, ex-situ cross-sectional SEM with EDXS mapping, and ex-situ XPS measurements were conducted for three electrodes after cycling Li||Li symmetric cells at 0.5 mA cm^{-2} and 30 °C with 0.5 mA h cm^{-2}, with the results displayed in **Figure 4**. The Nyquist plots for the LiF-, Mg-, and MgF_2-deposited electrodes, captured at different points of galvanostatic cycling in Figure 3d, are presented in Figure 4a–c, respectively; these results were fitted to the equivalent circuit model depicted in Figure S13,

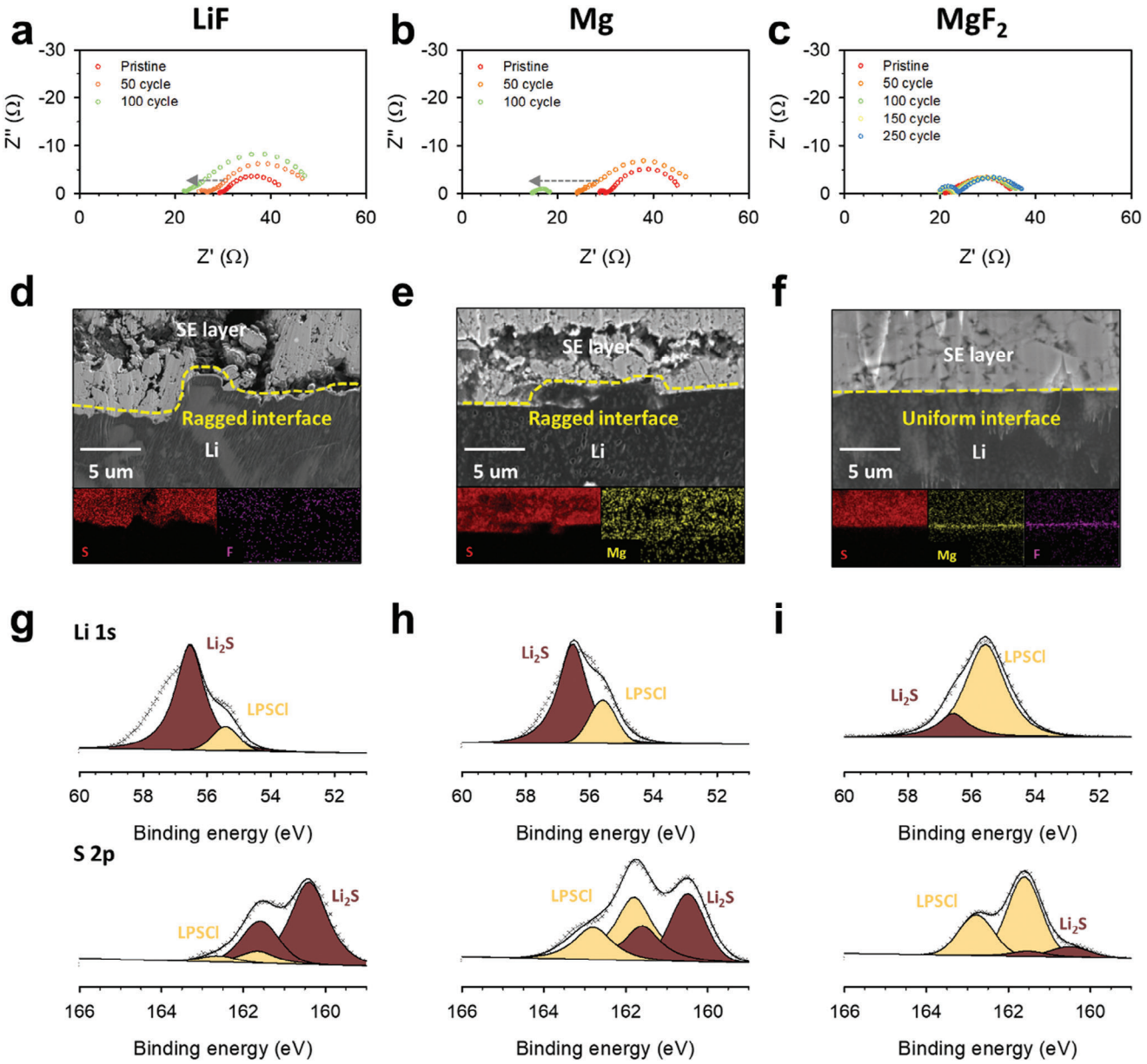

Figure 4. Interfacial evolution of LiF-, Mg-, and MgF_2-deposited LMAs before and after galvanostatic cycling of Li|LPSCl|Li symmetric cells. Nyquist plots of a) LiF-, b) Mg-, and c) MgF_2-coated LMAs at different points of cycling. Cross-sectional SEM images and corresponding EDXS maps of S, F, or Mg for d) LiF-, e) Mg-, and f) MgF_2-coated electrodes after 100 cycles. Corresponding ex-situ XPS signals of Li 1s and S 2p spectra for LPSCl pellets contacted with g) LiF-, h) Mg-, and i) MgF_2-deposited electrodes.

Supporting Information.[23] The high-frequency x-axis intercept values correspond to the bulk resistance of LPSCl, denoted as R_1. The cumulative medium- and low-frequency semicircle amplitudes ($R_2 + R_3$) signify the overall interfacial resistance between the Li metal and the SE.[61] The fitted values are summarized and plotted in Table S2 and Figure S14 (Supporting Information) respectively. The LiF- and Mg-deposited LMAs exhibited a substantial decrease in R_1 values with increasing cycle number, as indicated by the dashed arrows in Figure 4a,b. For LiF, the values reduced from 29.0 to 24.4 and 21.7 Ω after 50 and 100 cycles, respectively, whereas for Mg, they decreased from 28.8 to 23.9, and 14.7 Ω, indicating ISCs. The decreasing R_1 value is widely recognized as evidence of the penetration of Li into the SE bulk, closely aligning with the voltage drop observed in Figure 3d.[38] Furthermore, the ($R_2 + R_3$) values, originating from the interfacial instability, escalated upon cycling, from 14.2 to 21.2, and finally to 26.6 for LiF, and from 18.3 to 28.6, subsequently dropping to 3.9 after a hard short circuit for Mg. The increased interfacial resistance underscores the limited ability of LiF and Mg to suppress the side reactions. In contrast, MgF_2 exhibited far superior interfacial stability, maintaining nearly constant R_1 and ($R_2 + R_3$) values throughout 2000 h of galvanostatic cycling (Figure 4c; Figure S14, Supporting Information), demonstrating its ability to suppress both penetrating Li growth and Li-SSE side reactions.

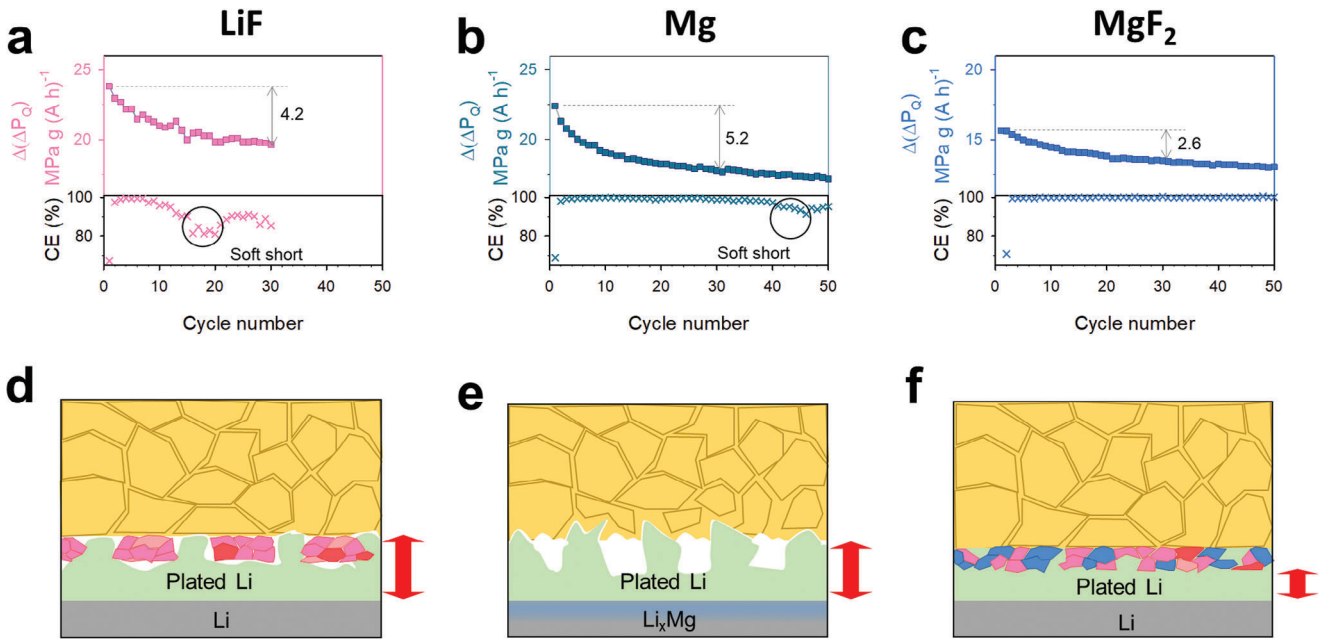

Figure 5. Operando electrochemical pressiometry (OEP) analysis results of NCM|LPSCl|Li all-solid-state full-cells employing LiF-, Mg-, and MgF_2-deposited LMAs at 0.3C and 30 °C. Capacity-normalized pressure change difference $\Delta(\Delta P_Q)$ and CE (coulombic efficiency) values for each cycle for a) LiF-, b) Mg-, and c) MgF_2-deposited LMAs. Schematic of interfacial Li plating/stripping mechanisms for d) LiF-, e) Mg-, and f) MgF_2-deposited LMAs. Note the reduced volume changes when more homogeneous Li^+ flux is achieved as depicted in (f).

Similar trends were observed in the cross-sectional SEM images and corresponding EDXS elemental maps after 100 galvanostatic cycles (Figure 4d–f). In contrast to the pristine interface depicted in Figure S15 (Supporting Information), the LiF- and Mg-deposited LMAs endured alternations, rendering the interfaces heterogeneous after cycling (Figure 4d,e, respectively). Pronounced penetration of Li metal and consequent crack propagation in the LPSCl layer were observed. Moreover, no clear indications of LiF or Li_xMg alloy layers were apparent in the EDXS maps after cycling. Owing to the extremely low content of Mg, the EDXS Mg map misleadingly showed more signals emanating from the SE layer compared to the Li metal (a more detailed discussion is available in the Supporting Information). The quantification derived from the EDXS analysis revealed that the actual Mg content in this sample was below the resolution of EDXS (Figure S16, Supporting Information). Significantly, both the cross-sectional SEM image and the corresponding EDXS maps confirmed that the MgF_2-coated LMAs sustained an intact interface even after 100 cycles (Figure 4f).

Ex situ XPS analysis was conducted to probe (electro)chemical interfacial evolution of the three electrode types. Figure 4g–i respectively present the Li 1s and S 2p XPS spectra of the LPSCl pellets derived from Li|LPSCl|Li symmetric cells employing LMAs deposited with LiF, Mg, and MgF_2 after 100 galvanostatic cycles. Notably, for both LiF- and Mg-deposited LMAs, the decomposition of LPSCl to Li_2S, a prevalent byproduct of the Li-LPSCl reaction, was evident in both Li 1s and S 2P spectra, with conspicuous signals of Li_2S (peaks at 56.5 eV for Li 1s and 160.5 eV for S 2p) and a concurrent diminution of the original LPSCl peaks (55.6 eV for Li 1s and 161.7 eV for S 2p).[62] In contrast, MgF_2 primarily preserves the fundamental characteristics of LPSCl, exhibiting only a marginal evolution toward Li_2S. A comparison of the signal area ratio of Li_2S to LPSCl reveals a stark contrast: LiF- and Mg-deposited LMAs recorded a markedly high ratio in both Li 1s (4.88 and 2.27) and S 2p (2.38 and 1.05), while MgF_2-coated LMAs registered notably lower ratios of 0.25 and 0.21, respectively (Table S3, Supporting Information), thereby substantiating the superior protective capabilities of the conversion-type MgF_2 coating layer.

The (electro)chemo-mechanical evolution was investigated using operando electrochemical pressiometry (OEP) analysis, utilizing NCM|LPSCl|Li ASLMB cells with LMAs deposited with LiF, Mg, and MgF_2 at ≈0.5 mA cm^{-2} and 30 °C, as illustrated in Figure S17 (Supporting Information). The dominant volume changes in LMAs, compared with those in NCM (4–6%), steered the overall pressure changes (ΔP), and the homemade pressure sensor records the pressure change during cycling as shown in Figure S18 (Supporting Information).[38,62] The pressure change difference values (Δ(ΔP)) (Figure S19, Supporting Information) were subsequently extracted and normalized per capacity at each cycle, denoted as $(\Delta(\Delta P_Q))$.[38] **Figure 5**a–c displays the $\Delta(\Delta P_Q)$ values, along with the corresponding Coulombic efficiency (CE), as a function of cycle numbers for LiF-, Mg-, and MgF_2-deposited LMAs in the NCM|Li full-cells.

First, initial $\Delta(\Delta P_Q)$ values for cells with LiF, Mg, and MgF_2 were recorded as 23.8, 22.4, and 15.6 MPa g $(A\ h)^{-1}$, respectively, maintaining the trend of higher $\Delta(\Delta P_Q)$ values for LiF and Mg than that of MgF_2 over successive cycles. The Li plating and stripping mechanisms for each electrode, as elucidated via OEP analysis, are illustrated in Figure 5d–f. Elevated $\Delta(\Delta P_Q)$ values for LiF and Mg, relative to MgF_2, imply a more pronounced volume change in the uniaxial direction, likely attributable to deficient (or uneven) interfacial contacts, as illustrated in Figure 5d,e.[38] Specifically, non-uniform contacts, such as imperfect physical

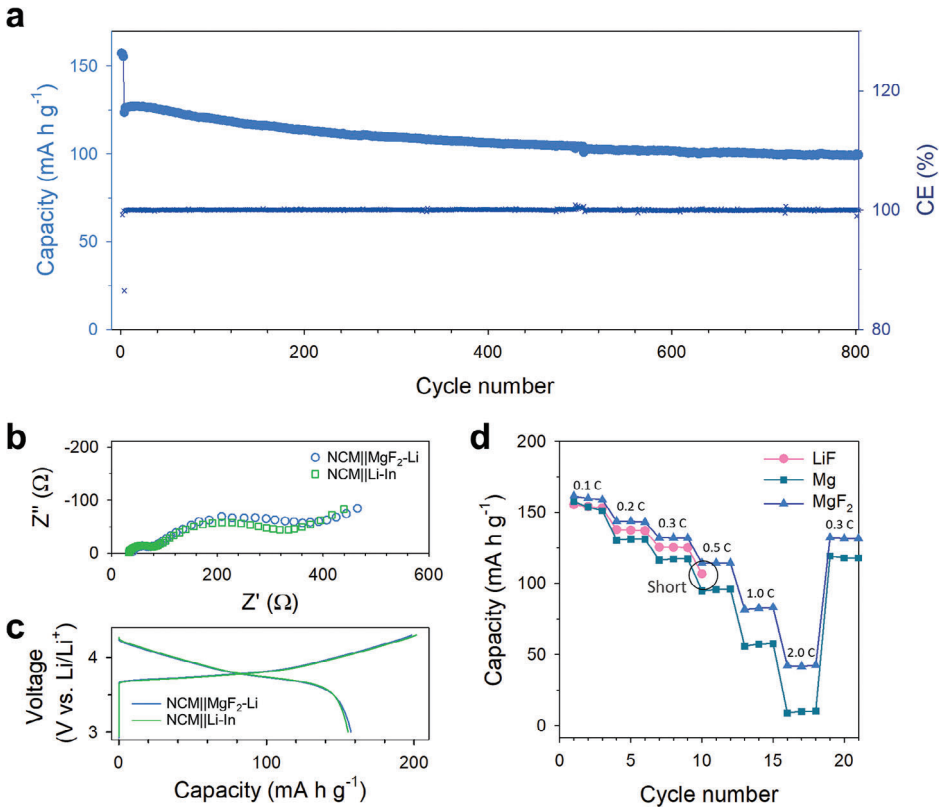

Figure 6. Electrochemical characterization of MgF_2-coated LMAs at 30 °C. a) Cycling performance results for MgF_2-deposited LMA in NCM|LPSCl|Li full cell. For cycling performance tests, cells were cycled at 0.1C for first three cycles and 0.3C for the subsequent cycles. b) Nyquist plots and c) first-cycle voltage profiles of NCM|LPSCl|Li cells employing MgF_2-coated LMA and NCM|LPSCl|Li-In cells. d) Rate capability results of NCM|LPSCl|Li full cells employing LiF-, Mg- and MgF_2- coated LMAs.

contact and the formation of a passivating layer, can induce current constriction, concentrating Li^+ ions onto restricted electrode areas, which, in turn, precipitate Li metal plating over a smaller area, thereby exerting higher pressure with an equivalent quantity of Li^+ ions. Owing to its extremely poor Li^+-conducting properties and susceptibility to mechanical damage, the LiF interlayer could potentially undergo current constriction (Figure 5d). Similarly, Mg-deposited LMAs were prone to current constriction owing to the absence (or lack) of protection (Figure 5e). In contrast, the MgF_2 coatings facilitated enhanced interfacial contact, resulting in a homogeneous Li^+ flux that can reduce the $\Delta(\Delta P_Q)$ values (Figure 5f). Secondly, the $\Delta(\Delta P_Q)$ values for cells with LiF and Mg exhibited substantial decreases after cycling, registering −4.2 and −5.2 MPa g $(A\ h)^{-1}$, respectively, after 30 cycles (Figures 5a,b), compared to the much milder decrease observed for cells with MgF_2, i.e. −2.6 MPa g $(A\ h)^{-1}$ (Figure 5c). The diminishing $\Delta(\Delta P_Q)$ upon cycling reflects the penetrating growth of Li through the SE layers.[38] In addition, e^--blocking effect of the in situ generated LiF layer has the potential in suppressing Li dendrite entrapment within bulk LPSCl,[43] thus contributing to the less decrease in $\Delta(\Delta P_Q)$. Consequently, the more modest reduction in $\Delta(\Delta P_Q)$ for MgF_2-coated LMAs, compared to those deposited with LiF or Mg, aligns with the EIS results in Figure 3a–c, thus confirming the superior efficacy of the MgF_2 deposition over LiF or Mg in inhibiting the penetrative Li growth.

The long-term cycling stability and rate capability of LMAs deposited with LiF, Mg, and MgF_2 in NCM|LPSCl|Li full-cells were evaluated at 30 °C, with the results presented in **Figures 6** and S20 (Supporting Information). The results of the long-term cycling performance are presented in Figures 6a and S20 (Supporting Information), with the corresponding charge–discharge voltage profiles across different cycles displayed in Figure S21 (Supporting Information). Specifically, MgF_2-coated LMAs delivered a high discharge capacity of 157 mA h $g^{-1}{}_{NCM}$ (at an initial cycle) at 0.1 C (and 121 mA h $g^{-1}{}_{NCM}$ at 0.3 C), subsequently achieving a stable cycle life extending up to 800 cycles with 82% capacity retention, indicating a notably enhanced performance compared to that of bare LMAs (Figure S22, Supporting Information). In comparative tests using NCM cathodes, MgF_2-coated LMAs showed similar performance to Li-In anodes, known for their superior compatibility with sulfide SEs.[11,14] This is indicated by marginal differences in Nyquist plots (Figure 6b) and voltage profiles (Figure 6c; Figure S23, Supporting Information), suggesting the effective compatibility of MgF_2-coated LMAs with LPSCl.

In contrast to MgF_2-coated LMAs, both the LiF- and Mg-deposited LMAs encountered ISCs at ≈30th cycle and exhibited a decline in the CE, concomitant with increasing charge capacities (Figure S21a,b, Supporting Information). Specifically, the LiF-coated LMAs display a dragging voltage profile during the charging step in the 30th cycle (Figure S21a, Supporting Information). Similarly, the Mg-deposited LMAs also presented an abnormally

elevated charge capacity, consequently yielding a reduced CE after 30 cycles, clearly indicating a soft ISC. During the rate capability tests, cells employing LiF-coated LMAs encountered ISC at 0.5 C (Figure 6c). Mg-deposited LMAs did not undergo ISC even at an escalated C-rate of up to 2.0 C. However, these Mg-deposited LMAs delivered substantially reduced discharge capacities, a phenomenon potentially correlated with the absence of an effective protective layer. In contrast, the MgF_2-LMAs did not exhibit ISCs and showed higher capacities, thereby affirming their superior capability in providing protective functionality.

Finally, we implemented MgF_2-LMAs in pouch-type NCM|LPSCL|Li ASLMBs (Figure S24, Supporting Information). These pouch cells demonstrated a notable discharge capacity of 182 mA h $g^{-1}{}_{NCM}$, along with 87% initial coulombic efficiency, at 0.2 C and 60 °C under a low pressure of 3 MPa. They also exhibited stable cycling performance over 30 cycles. These results highlight the potential of MgF_2-LMAs for practical applications.

3. Conclusion

In summary, we investigated LMAs deposited with LiF, Mg, and MgF_2 for ASLMBs employing SSEs, focusing on their formation and interfacial evolution. Control experiments, which compared conventional pressurized cells with the designed cells prepared with minimal or no pressure, provided the first demonstration that the LiF interlayer was compromised by the pressurization-based cell fabrication process, substantially nullifying its protective capacity. Direct Mg deposition onto Li metal led to the rapid diffusion of Mg into bulk Li, bypassing the formation of a conformal Mg layer and resulting in direct contact between the Li metal and the SSE (LPSCl). In contrast, the LiF and Li_xMg nanograins at the interfaces—formed through the conversion reaction of the MgF_2 coatings upon cycling—retained their conformality after cycling, thereby reinforcing their protective role. Capitalizing on this conversion-type feature, MgF_2-coated LMAs displayed markedly superior stability during continuous plating and stripping cycles, surpassing LiF- and Mg-deposited LMAs as well as bare LMAs. Through EIS, ex-situ cross-sectional SEM, and ex situ XPS analyses, the protective efficacy of the MgF_2 coatings in mitigating side reactions between Li metal and LPSCl and inhibiting Li metal penetrating growth was elucidated. Consistently, the NCM|LPSCl|Li full-cells utilizing MgF_2-coated LMAs markedly outperformed those with either LiF- or Mg-deposited LMAs in terms of rate capability and cycling performance. The OEP measurements substantiate that the MgF_2 coatings facilitate a uniform Li^+ flux and inhibit the growth of the penetrating Li metal. These findings have substantial implications, offering pivotal insights into the previously overlooked impact of cell assembly and operation on the interlayer design. Moreover, the essential beneficial aspects of the conversion-type interlayer are identified, thereby providing significant insights into the interfacial design of practical ASLMBs.

4. Experimental Section

Preparation of Materials: LiF (iTASCO), Mg (iTASCO), and MgF_2 (iTASCO) were used as received. The NCM powder was coated with $LiNbO_3$ (1.4 wt.%) via a wet-chemical method using lithium ethoxide (99.95%, Sigma Aldrich) and niobium ethoxide (99.95%, Sigma Aldrich).[63] Li_6PS_5Cl powder (CIS Co., Ltd. Korea) with a Li^+ conductivity of 2.8 mS cm^{-1} at 30 °C, as determined by the AC method using Ti|SE|Ti symmetric cells, was used as received.

Thermal Evaporation Deposition on Li Metal: For fabrication of LiF-, Mg-, and MgF_2-deposited Li metal electrodes, LiF, Mg, and MgF_2 were deposited onto Li metal foil with a thickness of 30 µm (SHIN HYUNG E&T CORP.) using a thermal evaporator (WOOSUNG HI-VAC Co.) housed within an Ar-filled glove box. The LiF, Mg, and MgF_2 granules were placed inside a Ta boat within the evaporator. All thermal evaporation depositions were conducted under a vacuum of $<10^{-6}$ torr at an evaporation rate of ≈0.5 Å s^{-1}. A thickness monitor was used to measure the thickness of the evaporated material, with the thickness adjusted to the actual thickness obtained through ellipsometry analysis using an ellipsometer (J. A. Woollam Co. Ltd.).

Material Characterization: Raman spectroscopy measurements were performed using a Raman Spectrometer (Horiba) with a laser wavelength of 473 nm. Cross-sectional SEM images were obtained by cold-polishing samples at 4.5 kV for 10 h, followed by 1.5 kV milling for 1 h with an Ar ion beam at −50 °C using IB19510CP (JEOL Ltd.). SEM images and the corresponding EDXS elemental maps were obtained using AURIGA (Carl Zeiss). The sample specimens were stored and transported using an air-isolation system holder to avoid exposure to ambient air. Ex situ XPS measurements were performed with a monochromatic Al K_α source (1486.6 eV) at 12 kV and 6 mA using K-Alpha+ (Thermo Fisher Scientific). The samples were mounted on a sample holder in an Ar-filled glove box and transferred to the XPS instrument without exposure to ambient air. TOFSIMS measurements were conducted using a TOF SIMS 5 (ION-TOF GmbH, Heisenbergstrabe, Munster) with a 30-keV pulsed Bi^{3+} ion source for the measurements and sputtering. DSIMS depth profiling was conducted using an IMS 7F-Auto (CAMECA) with a 5-keV pulsed Cs^+ ion source for the measurements and sputtering.

Electrochemical Characterization: All-solid-state cells with a diameter of 13 mm, comprising Ti rods as current collectors and a poly(aryl-ether-ether-ketone) (PEEK) mold, were used. To fabricate the all-solid-state Li|LPSCl|Li symmetric cells, an LPSCl layer was formed by pelletizing 150 mg of LPSCl by pressing at 370 MPa. LMAs with diameters of 12 mm were placed on both sides of the LPSCl pellet. The entire assembly was pressed at 70 MPa. An external pressure of 7 MPa was applied during cycling. After pre-cycling at 0.2 mA cm^{-2} for 1 h for each charge and discharge cycle during the first 10 cycles, galvanostatic cycling tests were carried out at 0.5 mA cm^{-2} for 1 h at each charge and discharge cycle. EIS data were collected at an amplitude of 7 mV and a frequency range of 10 mHz to 7 MHz using a VSP300 (Bio-Logic). EIS measurements of the symmetric cells were performed before the galvanostatic cycling test and after 50, 100, 150, and 250 cycles. NCM cathodes were prepared using the wet slurry method. A mixture of NCM, LPSCl, nitrile butadiene rubber, and conducting carbon additives (Super C65) in a weight ratio of 70.0:27.5:1.5:1.0 was added to a slurry processing solvent of benzyl acetate (99%, Sigma Aldrich) and coated on a carbon-coated Al current collector using the doctor-blade method. The cast slurry was dried under vacuum at 150 °C. The mass loadings of NCM were 13–14 mg cm^{-2}. After the SE layers were formed by pelletizing 150 mg of the LPSCl powder at 70 MPa, the composite cathodes were placed on one side of the SE layer, and the entire assembly was pressed at 370 MPa. Finally, LMA was attached to the other side of the SE layer at 70 MPa. An external pressure of 15 MPa was applied during cycling. All-solid-state full-cells were cycled at 0.1C for the initial three cycles and then at 0.3 C for subsequent cycles between 3.0–4.3 V (vs Li/Li^+) at 30 °C. For OEP measurements, NCM|Li full-cells were cycled at 0.3C and 30 °C. For the fabrication of NCM|Li-In cells, Li–In electrodes, which were partially lithiated indium (nominal composition of $Li_{0.5}In$), were prepared by mixing Li (FMC Lithium Corp.) and In (99%, Sigma Aldrich) powders. After the SE layers were formed by pelletizing 150 mg of the LPSCl powders, a Li-In electrode ($Li_{0.5}In$) was placed on one side of the SE layer. After placing the as-prepared cathode electrode on the other side of the SE layer, the assemblies were pressed at 370 MPa. Pressure sensors with a resolution of 0.1 kg (load cell, BONGSHIN) were

placed in a customized ASLMB set-up for OEP measurement (Figure S18, Supporting Information).[64] The pressure changes during charging and discharging were monitored using in-house software. For the fabrication of NCM|LPSCl|Li pouch-type full cells, an LPSCl film with a composition of 97:3 (LPSCl/nitrile butadiene rubber (NBR) weight ratio) was prepared via doctor-blade method.[65,66] Following this, the SE film and NCM cathode were attached using cold isostatic press (CIP) at 450 MPa. Afterward, LMA was placed on the other side of the SE film. The entire assembly was then sealed within a pouch and subjected to pressurization at 100 MPa using CIP. Galvanostatic charge–discharge cycling tests for pouch-type ASLMBs were conducted at 60 °C, 0.2 C, and 3 MPa. All the electrodes were fabricated in an Ar-filled dry glove box.

Supporting Information

Supporting Information is available from the Wiley Online Library or from the author.

Acknowledgements

This work was supported by the Technology Innovation Program (20012216) funded by the Ministry of Trade, Industry & Energy (MOTIE, Korea), and by the program of phase development of carbon neutral technologies thorugh the National Research Foundation of Korea (NRF) funded by the Ministry of Science and ICT (NRF-2022M3J1A1085397).

Conflict of Interest

The authors declare no conflict of interest.

Data Availability Statement

The data that support the findings of this study are available from the corresponding author upon reasonable request.

Keywords

lithium metal anodes, protective interlayers, solid-state batteries, sulfide solid electrolytes, thermal evaporation deposition

Received: November 5, 2023
Revised: December 19, 2023
Published online: January 18, 2024

[1] Y.-G. Lee, S. Fujiki, C. Jung, N. Suzuki, N. Yashiro, R. Omoda, D.-S. Ko, T. Shiratsuchi, T. Sugimoto, S. Ryu, J. H. Ku, T. Watanabe, Y. Park, Y. Aihara, D. Im, I. T. Han, *Nat. Energy* **2020**, *5*, 299.
[2] T. Krauskopf, F. H. Richter, W. G. Zeier, J. Janek, *Chem. Rev.* **2020**, *120*, 7745.
[3] H. Li, *Joule* **2019**, *3*, 911.
[4] Y. S. Jung, D. Y. Oh, Y. J. Nam, K. H. Park, *Isr. J. Chem.* **2015**, *55*, 472.
[5] J. W. Choi, D. Aurbach, *Nat. Rev. Mater.* **2016**, *1*, 16013.
[6] D. Lin, Y. Liu, Y. Cui, *Nat. Nanotechnol.* **2017**, *12*, 194.
[7] K. H. Park, Q. Bai, D. H. Kim, D. Y. Oh, Y. Zhu, Y. Mo, Y. S. Jung, *Adv. Energy Mater.* **2018**, *8*, 1800035.
[8] R. Murugan, V. Thangadurai, W. Weppner, *Angew. Chem. Int. Ed. Engl.* **2007**, *46*, 7778.
[9] H.-J. Deiseroth, S.-T. Kong, H. Eckert, J. Vannahme, C. Reiner, T. Zaiß, M. Schlosser, *Angew. Chem. Int Ed. Engl.* **2008**, *47*, 755.
[10] L. Duchêne, A. Remhof, H. Hagemann, C. Battaglia, *Energy Stor. Mater.* **2020**, *25*, 782.
[11] H. Kwak, D. Han, J. Lyoo, J. Park, S. H. Jung, Y. Han, G. Kwon, H. Kim, S. T. Hong, K. W. Nam, Y. S. Jung, *Adv. Energy Mater.* **2021**, *11*, 2003190.
[12] L. Zhou, N. Minafra, W. G. Zeier, L. F. Nazar, *Acc. Chem. Res.* **2021**, *54*, 2717.
[13] H. Kwak, S. Wang, J. Park, Y. Liu, K. T. Kim, Y. Choi, Y. Mo, Y. S. Jung, *ACS Energy Lett.* **2022**, *7*, 1776.
[14] H. Kwak, J.-S. Kim, D. Han, J. S. Kim, J. Park, G. Kwon, S.-M. Bak, U. Heo, C. Park, H.-W. Lee, K.-W. Nam, D.-H. Seo, Y. S. Jung, *Nat. Commun.* **2023**, *14*, 2459.
[15] C. Wang, K. Fu, S. P. Kammampata, D. W. Mcowen, A. J. Samson, L. Zhang, G. T. Hitz, A. M. Nolan, E. D. Wachsman, Y. Mo, V. Thangadurai, L. Hu, *Chem. Rev.* **2020**, *120*, 4257.
[16] T. Thompson, S. Yu, L. Williams, R. D. Schmidt, R. Garcia-Mendez, J. Wolfenstine, J. L. Allen, E. Kioupakis, D. J. Siegel, J. Sakamoto, *ACS Energy Lett.* **2017**, *2*, 462.
[17] Y. Kato, S. Hori, T. Saito, K. Suzuki, M. Hirayama, A. Mitsui, M. Yonemura, H. Iba, R. Kanno, *Nat. Energy* **2016**, *1*, 16030.
[18] J. Kasemchainan, S. Zekoll, D. Spencer Jolly, Z. Ning, G. O. Hartley, J. Marrow, P. G. Bruce, *Nat. Mater* **2019**, *18*, 1105.
[19] A. Banerjee, X. Wang, C. Fang, E. A. Wu, Y. S. Meng, *Chem. Rev.* **2020**, *120*, 6878.
[20] Z. Ning, D. S. Jolly, G. Li, R. De Meyere, S. D. Pu, Y. Chen, J. Kasemchainan, J. Ihli, C. Gong, B. Liu, D. L. R. Melvin, A. Bonnin, O. Magdysyuk, P. Adamson, G. O. Hartley, C. W. Monroe, T. J. Marrow, P. G. Bruce, *Nat. Mater.* **2021**, *20*, 1121.
[21] Z. Ning, G. Li, D. L. R. Melvin, Y. Chen, J. Bu, D. Spencer-Jolly, J. Liu, B. Hu, X. Gao, J. Perera, C. Gong, S. D. Pu, S. Zhang, B. Liu, G. O. Hartley, A. J. Bodey, R. I. Todd, P. S. Grant, D. E. J. Armstrong, T. J. Marrow, C. W. Monroe, P. G. Bruce, *Nature* **2023**, *618*, 287.
[22] L. Ye, X. Li, *Nature* **2021**, *593*, 218.
[23] S. Wenzel, S. J. Sedlmaier, C. Dietrich, W. G. Zeier, J. Janek, *Solid State Ion* **2018**, *318*, 102.
[24] Y. Zhu, X. He, Y. Mo, *ACS Appl. Mater. Interfaces* **2015**, *7*, 23685.
[25] J. A. Lewis, F. J. Q. Cortes, Y. Liu, J. C. Miers, A. Verma, B. S. Vishnugopi, J. Tippens, D. Prakash, T. S. Marchese, S. Y. Han, C. Lee, P. P. Shetty, H. W. Lee, P. Shevchenko, F. De Carlo, C. Saldana, P. P. Mukherjee, M. T. McDowell, *Nat. Mater* **2021**, *20*, 503.
[26] H. Wan, Z. Wang, S. Liu, B. Zhang, X. He, W. Zhang, C. Wang, *Nat. Energy* **2023**, *8*, 473.
[27] E. Kazyak, M. J. Wang, K. Lee, S. Yadavalli, A. J. Sanchez, M. D. Thouless, J. Sakamoto, N. P. Dasgupta, *Matter* **2022**, *5*, 3912.
[28] K. Lee, E. Kazyak, M. J. Wang, N. P. Dasgupta, J. Sakamoto, *Joule* **2022**, *6*, 2547.
[29] F. Han, A. S. Westover, J. Yue, X. Fan, F. Wang, M. Chi, D. N. Leonard, N. J. Dudney, H. Wang, C. Wang, *Nat. Energy* **2019**, *4*, 187.
[30] X. Liu, R. Garcia-Mendez, A. R. Lupini, Y. Cheng, Z. D. Hood, F. Han, A. Sharafi, J. C. Idrobo, N. J. Dudney, C. Wang, C. Ma, J. Sakamoto, M. Chi, *Nat. Mater.* **2021**, *20*, 1485.
[31] D. K. Singh, A. Henss, B. Mogwitz, A. Gautam, J. Horn, T. Krauskopf, S. Burkhardt, J. Sann, F. H. Richter, J. Janek, *Cell Rep.* **2022**, *3*, 101043.
[32] J. Su, M. Pasta, Z. Ning, X. Gao, P. G. Bruce, C. R. M. Grovenor, *Energy Environ. Sci.* **2022**, *15*, 3805.
[33] X. Fan, X. Ji, F. Han, J. Yue, J. Chen, L. Chen, T. Deng, J. Jiang, C. Wang, *Sci. Adv.* **2018**, *4*, eaau9245.
[34] H. Xu, Y. Li, A. Zhou, N. Wu, S. Xin, Z. Li, J. B. Goodenough, *Nano Lett.* **2018**, *18*, 7414.
[35] J. Li, Y. Li, S. Zhang, T. Liu, D. Li, L. Ci, *ACS Appl. Mater. Interfaces* **2022**, *14*, 55727.
[36] K. K. Fu, Y. Gong, B. Liu, Y. Zhu, S. Xu, Y. Yao, W. Luo, C. Wang, S. D. Lacey, J. Dai, Y. Chen, Y. Mo, E. Wachsman, L. Hu, *Sci. Adv.* **2017**, *3*, e1601659.

[37] A. Kato, H. Kowada, M. Deguchi, C. Hotehama, A. Hayashi, M. Tatsumisago, *Solid State Ion* **2018**, *322*, 1.
[38] H. Lim, S. Jun, Y. B. Song, H. Bae, J. H. Kim, Y. S. Jung, *Energy Stor. Mater.* **2022**, *50*, 543.
[39] F. Zhao, Q. Sun, C. Yu, S. Zhang, K. Adair, S. Wang, Y. Liu, Y. Zhao, J. Liang, C. Wang, X. Li, X. Li, W. Xia, R. Li, H. Huang, L. Zhang, S. Zhao, S. Lu, X. Sun, *ACS Energy Lett.* **2020**, *5*, 1035.
[40] X. Shi, Y. Pang, B. Wang, H. Sun, X. Wang, Y. Li, J. Yang, H.-W. Li, S. Zheng, *Mater. Today Nano* **2020**, *10*, 100079.
[41] D. Lin, Y. Liu, W. Chen, G. Zhou, K. Liu, B. Dunn, Y. Cui, *Nano Lett.* **2017**, *17*, 3731.
[42] L. Chen, K.-S. Chen, X. Chen, G. Ramirez, Z. Huang, N. R. Geise, H.-G. Steinrück, B. L. Fisher, R. Shahbazian-Yassar, M. F. Toney, M. C. Hersam, J. W. Elam, *ACS Appl. Mater. Interfaces* **2018**, *10*, 26972.
[43] S. Lee, K.-S. Lee, S. Kim, K. Yoon, S. Han, M. H. Lee, Y. Ko, J. H. Noh, W. Kim, K. Kang, *Sci. Adv.* **2022**, *8*, eabq0153.
[44] T. Wang, J. Duan, B. Zhang, W. Luo, X. Ji, H. Xu, Y. Huang, L. Huang, Z. Song, J. Wen, C. Wang, Y. Huang, J. B. Goodenough, *Energy Environ. Sci.* **2022**, *15*, 1325.
[45] Y. Liu, C. Li, B. Li, H. Song, Z. Cheng, M. Chen, P. He, H. Zhou, *Adv. Energy Mater.* **2018**, *8*, 1702374.
[46] S. Kim, G. Yoon, S.-K. Jung, S. Park, J.-S. Kim, K. Yoon, S. Lee, K. Kang, *ACS Energy Lett.* **2022**, *8*, 9.
[47] A. C. Thenuwara, E. L. Thompson, T. F. Malkowski, K. D. Parrotte, K. E. Lostracco, S. Narayan, R. T. Rooney, L. A. Seeley, M. R. Borges, B. D. Conway, Z. Song, M. E. Badding, K. G. Gallagher, *ACS Energy Lett.* **2023**, *8*, 4016.
[48] K. Yan, Z. Lu, H.-W. Lee, F. Xiong, P.-C. Hsu, Y. Li, J. Zhao, S. Chu, Y. Cui, *Nat. Energy* **2016**, *1*, 16010.
[49] T. Krauskopf, B. Mogwitz, C. Rosenbach, W. G. Zeier, J. Janek, *Adv. Energy Mater* **2019**, *9*, 1902568.
[50] J. Oh, S. H. Choi, J. Y. Kim, J. Lee, T. Lee, N. Lee, T. Lee, Y. Sohn, W. J. Chung, K. Y. Bae, S. Son, J. W. Choi, *Adv. Energy Mater.* **2023**, 2301508.
[51] M. Siniscalchi, J. Liu, J. S. Gibson, S. J. Turrell, J. Aspinall, R. S. Weatherup, M. Pasta, S. C. Speller, C. R. M. Grovenor, *ACS Energy Lett.* **2022**, *7*, 3593.
[52] L. Zhao, W. Li, C. Wu, Q. Ai, L. Guo, Z. Chen, J. Zheng, M. Anderson, H. Guo, J. Lou, Y. Liang, Z. Fan, J. Zhu, Y. Yao, *Adv. Energy Mater.* **2023**, *13*, 2300679.
[53] H. Wan, S. Liu, T. Deng, J. Xu, J. Zhang, X. He, X. Ji, X. Yao, C. Wang, *ACS Energy Lett.* **2021**, *6*, 862.
[54] J. Lee, S. H. Choi, G. Im, K. J. Lee, T. Lee, J. Oh, N. Lee, H. Kim, Y. Kim, S. Lee, J. W. Choi, *Adv. Mater* **2022**, *34*, e2203580.
[55] M.-H. Kim, T.-U. Wi, J. Seo, A. Choi, S. Ko, J. Kim, U. Jung, M. S. Kim, C. Park, S. Jin, H.-W. Lee, *Nano Lett.* **2023**, *23*, 3582.
[56] W. Zhong, J.-C. Zhao, *Mater* **2020**, *11*, 100674.
[57] G. Guo, H. Zhou, Q. Wang, J. Wang, J. Tan, J. Li, P. Jin, H. Shen, *Nanoscale* **2017**, *9*, 875.
[58] R. S. Krishnan, J. P. Russell, *Brit. J. Appl. Phys.* **1966**, *17*, 501.
[59] L. L. Kong, L. Wang, Z. C. Ni, S. Liu, G. R. Li, X. P. Gao, *Adv. Funct. Mater.* **2019**, *29*.
[60] Y. Lu, C.-Z. Zhao, H. Yuan, X.-B. Cheng, J.-Q. Huang, Q. Zhang, *Adv. Funct. Mater.* **2021**, *31*, 2009925.
[61] J. Luo, Q. Sun, J. Liang, K. Adair, F. Zhao, S. Deng, Y. Zhao, R. Li, H. Huang, R. Yang, S. Zhao, J. Wang, X. Sun, *ACS Energy Lett.* **2023**, *8*, 3676.
[62] Y. Han, S. H. Jung, H. Kwak, S. Jun, H. H. Kwak, J. H. Lee, S. T. Hong, Y. S. Jung, *Adv. Energy Mater.* **2021**, *11*, 2100216.
[63] D. Y. Oh, Y. J. Nam, K. H. Park, S. H. Jung, K. T. Kim, A. R. Ha, Y. S. Jung, *Adv. Energy Mater.* **2019**, *9*, 1802927.
[64] S. Jun, Y. J. Nam, H. Kwak, K. T. Kim, D. Y. Oh, Y. S. Jung, *Adv. Funct. Mater.* **2020**, *30*, 2002535.
[65] Y. J. Nam, S.-J. Cho, D. Y. Oh, J.-M. Lim, S. Y. Kim, J. H. Song, Y.-G. Lee, S.-Y. Lee, Y. S. Jung, *Nano Lett.* **2015**, *15*, 3317.
[66] Y. B. Song, K. H. Baeck, H. Kwak, H. Lim, Y. S. Jung, *Adv. Ener. Mater.* **2023**, *13*, 2301142.